scientific reports

Check for updates

OPEN

# Towards device stability of perovskite solar cells through low-cost alkyl-terminated SFX-based hole transporting materials and carbon electrodes

Jeeranun Manit[1], Pongsakorn Kanjanaboos[2], Phiphob Naweephattana[1], Atittaya Naikaew[2], Ladda Srathongsian[2], Chaowaphat Seriwattanachai[2], Ratchadaporn Supruangnet[5], Hideki Nakajima[5], Utt Eiamprasert[3] & Supavadee Kiatisevi[1,4]✉

**Developing cost-effective, high-efficiency, and stable hole transporting materials (HTMs) is crucial for replacing traditional spiro-OMeTAD in perovskite solar cells (PSCs) and achieving sustainable solar energy solutions. This work presents two novel air-stable HTMs based on a spiro[fluorene-9,9′-xanthene] (SFX) core functionalized with *N*-methylcarbazole (XC2-M) and *N*-hexylcarbazole (XC2-H) rings. These HTMs were synthesized via a straightforward, three-step process with good overall yields (~40%) and low production costs. To further reduce device cost, carbon back electrodes were employed. The resulting PSCs, with a structure of FTO/$SnO_2$/$Cs_{0.05}FA_{0.73}MA_{0.22}Pb(I_{0.77}Br_{0.23})_3$/HTM/C achieved power conversion efficiencies (PCEs) of 13.5% (XC2-M) and 10.2% (XC2-H), comparable to the reference spiro-OMeTAD device (12.2%). The choice of alkyl chain on the HTM significantly impacts film morphology and device stability. The XC2-H device exhibited exceptional long-term stability, retaining approximately 90% of its initial PCE after 720 h of storage in 30–40% humidity air without encapsulation. This surpasses the performance of both the spiro-OMeTAD (55% retention) and XC2-M (68% retention) devices. The superior stability of XC2-H is attributed to its highly hydrophobic nature and the formation of a compact, smooth film due to interdigitation of the hexyl chains. The straightforward synthesis of XC2-H from commercially available materials offers a promising approach for large-scale PSC production.**

**Keywords** Perovskite solar cell, Hole transporting material, Spiro[fluorene-9,9'-xanthene], Carbon electrode, Carbazole

Over the past decade, perovskite solar cells (PSCs) have made tremendous progresses in photovoltaic efficiency comparable to crystalline silicon solar cells after the discovery of the efficient $TiO_2$ sensitization by organolead halide perovskite for visible-light conversion into electricity in 2009 by Miyasaka and co-workers[1]. The power conversion efficiency (PCE) record for PSCs currently exceeds 26.2%[2]. The efficiency and stability of the devices are mainly affected by the PSC structure as well as the ability of charge transporting materials, particularly HTMs. The functions of HTMs are as follows: (i) extracting photogenerated holes as a result of the HOMO of the HTM which is located above the valence band of the perovskite; (ii) transporting the holes to electrodes and blocking a direct contact between the perovskite layer and the electrode; and (iii) suppressing nonradiative recombination[3].

Efficient HTMs should have following properties such as (i) being cost-effective and simply synthesized which are significant for the practical development of PSCs, (ii) possessing appropriate HOMO and LUMO

[1]Department of Chemistry, Faculty of Science, Mahidol University, Rama VI Rd, Ratchathewi, Bangkok 10400, Thailand. [2]School of Materials Science and Innovation, Faculty of Science, Mahidol University, Nakhon Pathom 73170, Thailand. [3]Department of Chemistry, Faculty of Science and Technology, Rajamangala University of Technology Thanyaburi, Pathum Thani 12110, Thailand. [4]Center of Sustainable Energy and Green Materials, Faculty of Science, Mahidol University, Putthamonthon, Nakhon Pathom 73170, Thailand. [5]Synchrotron Light Research Institute, Nakhon Ratchasima 30000, Thailand. ✉email: supavadee.mon@mahidol.edu

energy levels relative to the valence band energy level of the perovskite, (iii) showing a good thermal stability and hydrophobicity to prevent degradation and enhance long-term device stability, as well as good solubility in film formation, and (iv) having an intrinsically high hole mobility and a high hole conductivity.

In general, HTMs can be categorized into three types; inorganic, polymeric, and small-organic molecule HTMs. Although the inorganic materials have high stability, high internal hole mobility, and low material cost[4], solvents commonly used for their deposition are likely to dissolve the perovskite layer resulting in reduced device stability[5]. Polymeric HTMs such as poly(triarylamine) (PTAA) and polyaniline (PANI) seem to present a high hole mobility for PSCs and good film-forming properties[6]. However, their limitations such as difficult purification, low solubility, and broad molecular weight distribution lead to the development of organic materials to meet industry requirements. Small-organic molecule HTMs offer potential advantages such as simple purification, flexible molecular structure, controllable molecular weight, and manageable production costs. Additional significant properties such as good solubility and high thermal stability can be achieved by using the small-organic molecule HTMs with a non-planar 3D geometry, as featured by the widely used spiro-OMeTAD which contains a spirobifluorene (SBF) core unit. However, low mobility ($\approx 10^{-5}$ $cm^2V^{-1}s^{-1}$), limited conductivity ($\approx 10^{-7}$ $Scm^{-1}$),[7,8] high cost (~90 to ~460 USD per gram depending on its purity)[9], and synthetic complexity of spiro-OMeTAD make large-scale production impractical. Therefore, the need to develop alternative HTMs with cost-effectiveness, high efficiency, and good stability for sustainable PSCs remains a challenge to be addressed.

Recently, various conjugated moieties and structures similar to spiro-OMeTAD have been used to improve the hole mobility of organic HTMs including the efficiency and stability of PSCs[3,10,11]. A spiro-based HTM that proves 20% PCE is found to be characterized by spiro[fluorene-9,9'-xanthene] (SFX) as the core skeleton[12–17]. SFX is known for its concise and economic synthesis through a one-pot reaction between phenol and fluorenone[18–20]. Furthermore, SFX-OMeTAD was found to exhibit much faster dissolution than spiro-OMeTAD. The performances of PSCs based on SFX derivatives reportedly range from 12.4 to 20.8% comparable to those based on SBF[12–16].

Carbazole-based HTMs have demonstrated remarkable potential in PSCs, achieving PCEs of up to 17−21%.[21–23] Notably, an SBF-based HTM incorporating an extended π-conjugated *N*-ethylcarbazole unit exhibited an impressive PCE of 21.76%.[23] The presence of the ethyl side chain effectively alleviated unfavorable phase-separation in the film, reduced π−π stacking interactions, and enhanced solubility.

With the goal of developing alternative HTMs with cost-effectiveness, high efficiency, and good stability for PSCs, we designed two new SFX-based HTMs by introducing carbazole motifs with two different alkyl groups as peripheral substituents. These HTMs, **XC2-M** ($N^2$,$N^7$-bis(4-methoxyphenyl)-$N^2$,$N^7$-bis(9-methyl-9H-carbazol-3-yl)spiro[fluorene-9,9'-xanthene]-2,7-diamine) and **XC2-H** ($N^2$,$N^7$-bis(9-hexyl-9H-carbazol-3-yl)-$N^2$,$N^7$-bis(4-methoxyphenyl)spiro[fluorene-9,9'-xanthene]-2,7-diamine), exhibit a distinctive butterfly-shaped structure as depicted in Fig. 1. In order to further reduce the cost of PSCs, we used a carbon (C) electrode instead of Au or Ag due to its abundant source, low cost, and efficient charge collection with a proper work function (WF) of −5 eV similar to that of Au[24,25]. Although the performance of carbon-based PSCs is notably less efficient compared to devices employing a metal-based electrode, the highly hydrophobic nature and chemical inertness of the carbon electrode are reportedly advantageous for the long-term stability of PSCs without the need for encapsulation[23].

With the introduction of methyl and hexyl groups, the **XC2-M** and **XC2-H** based devices using the carbon electrode and $Cs_{0.05}FA_{0.73}MA_{0.22}Pb(I_{0.77}Br_{0.23})_3$ (triple-cation perovskite) showed short-circuit photocurrent densities ($J_{SC}$) of 22.2 mA $cm^{-2}$ and 21.1 mA $cm^{-2}$, and fill factors (FF) of 0.64 and 0.48, yielding the PCEs of 13.5% and 10.2%, respectively. The **XC2-H**-based device without encapsulation exhibits remarkable stability, retaining 88% of its original power conversion efficiency (PCE) after 720 h of storage in 30−40% humidity-controlled air at ambient temperature. In contrast, devices based on the reference spiro-OMeTAD and **XC2-M** retain only 55% and 68% of their initial PCEs under the same conditions, respectively. Additionally, after annealing at 65 °C for 720 h, the **XC2-H**-based device retains approximately 40% of its initial PCE. This stability is significantly superior to **XC2-M**- and spiro-OMeTAD-based devices, which retain only 20% and 5% of their initial PCEs, respectively, and underscores the advantage of incorporating long alkyl chains into HTM design, providing a viable approach to address both film formation and stability issues.

## Experimental

### Materials

Commercially available reagents were purchased from Sigma-Aldrich, TCI and used without further purification. Toluene was freshly distilled from sodium prior to use. Other solvents were used directly. $Pd_2(dba)_3$ and dicyclohexyl[2′,4′,6′-tris(propan-2-yl)[1,1′-biphenyl]-2-yl]phosphane (Xphos) were purchased from Sigma Aldrich. Chromatography was performed using Merck silica gel (60 Å, 70−230 mesh). Nuclear Magnetic Resonance (NMR) spectra were recorded on a Bruker Ascend™ 400 MHz spectrometer using $CDCl_3$ and DMSO-$d_6$ as solvents. Tetramethylsilane (TMS) and non-deuterated residue solvents were used as internal standards. High-resolution mass spectra (HRMS) were recorded with an HR-TOF-MS Micromass model VQTOF2 mass spectrometer and reported in m/z unit. UV−vis absorption spectra were recorded in $CH_2Cl_2$ solution at room temperature on Shimadzu UV-2600 spectrophotometer. The UV−vis absorption spectra of the HTMs in thin film state were recorded using an Ocean Optics DH-2000-BAL light source. The emission spectra were recorded in $CH_2Cl_2$ solution on a HORIBA FluoroMax® Plus. Steady-state photoluminescence (PL) spectra were obtained using either a SHIMADZU RF-5301PC or Edinburgh Instruments FLS980 spectrometer. PL spectra were measured using an integration time of 0.1 s, an excitation wavelength of 625 nm, excitation and emission slit widths of 10 nm and 5 nm, respectively, and an emission range of 650–850 nm. Cyclic voltammetry (CV) measurements were performed on an electrochemical workstation (CH Instrument model 620E voltammetric

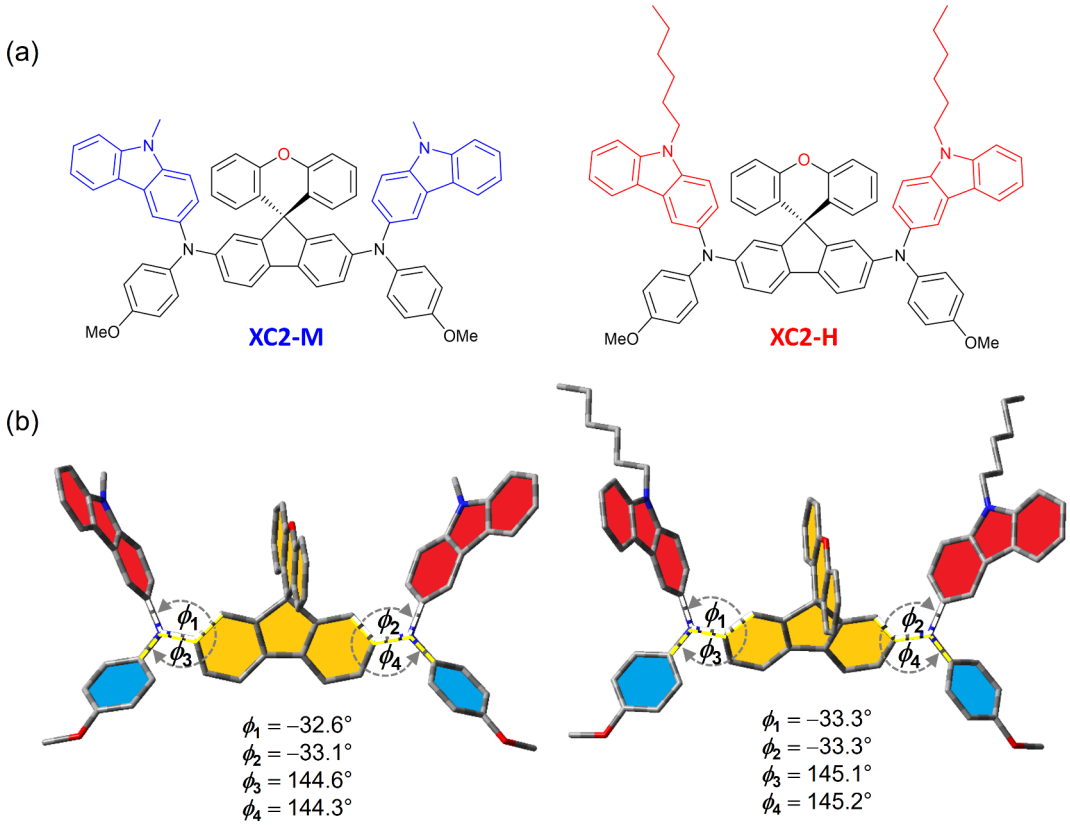


**Fig. 1**. **(a)** Chemical structures of the HTMs, **XC2-M** and **XC2-H**. (**b)** Optimized molecular geometries of **XC2-M** and **XC2-H** obtained by DFT calculations at B3LYP/6-31G(d) in dichloromethane as the solvent parameter.

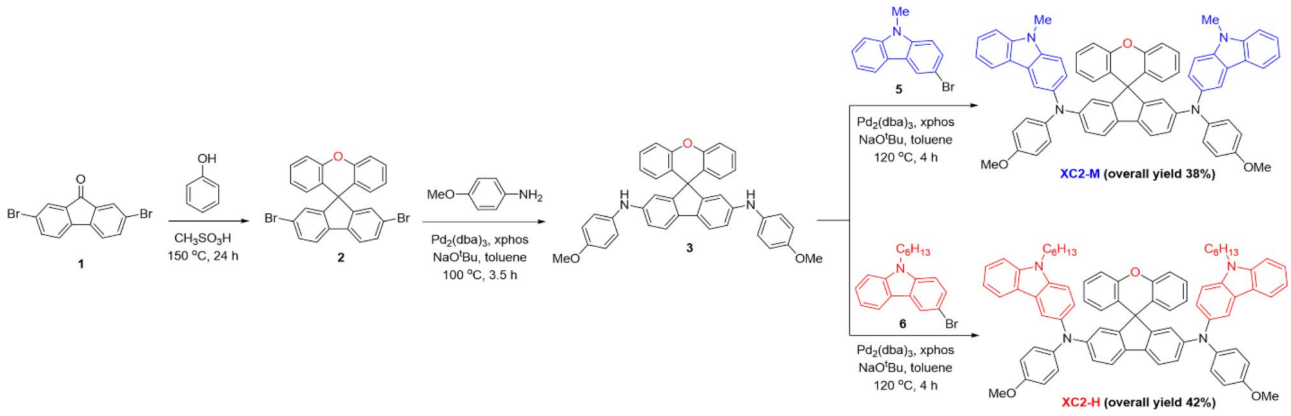


**Fig. 2**. Synthesis of **XC2-M** and **XC2-H**.

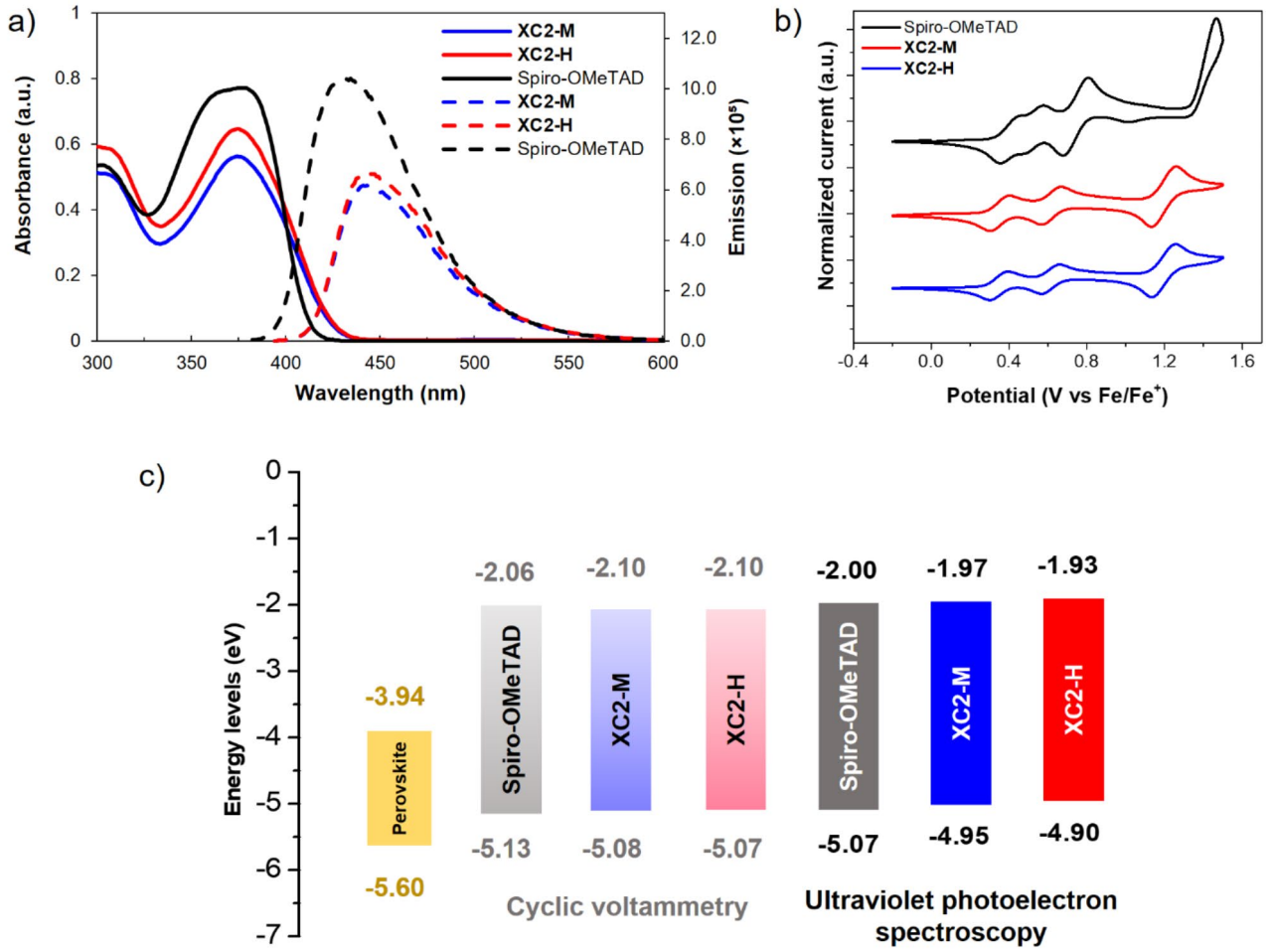


**Fig. 3**. (**a**) Absorption (solid line) and emission (dash line) spectra of **XC2-M** (blue), **XC2-H** (red), and spiro-OMeTAD (black) in acetonitrile. (**b**) CV results of **XC2-M**, **XC2-H**, and spiro-OMeTAD ($10^{-4}$ M in dichloromethane). (**c**) Energy level diagram of **XC2-M** and **XC2-H** in comparison with perovskite and spiro-OMeTAD measured by CV and UPS techniques.

| HTMs | $\lambda_{max,abs}$ [a] [nm] | $\lambda_{max,em}$ [a] [nm] | $\lambda_{int}$ [b] [nm] | $E_g$ [c] [eV] | $E^{ox}_{onset}$ [eV] | $E_{HOMO}$ [eV] | $E_{LUMO}$ [eV] | μ [$cm^2V^{-1}s^{-1}$] |
|---|---|---|---|---|---|---|---|---|
| **XC2-M** | 374 | 433 | 416 | 2.98 | 0.28 | −5.08[e]/−4.95[f] | −2.10[e]/−1.97[f] | $2.67\times10^{-3}$ |
| **XC2-H** | 374 | 433 | 417 | 2.97 | 0.27 | −5.07[e]/−4.90[f] | −2.10[e]/−1.93[f] | $1.27\times10^{-3}$ |
| Spiro-OMeTAD | 377 | 430 | 404 | 3.07 | 0.33 | −5.13[e]/−5.07[f] | −2.06[e]/−2.00[f] | $2.55\times10^{-3}$ |

**Table 1**. Summary of spectroscopic and photophysical data, oxidation potential, and hole mobility of **XC2-M**, **XC2-H**, and spiro-OMeTAD. [a]$\lambda_{max,abs}$ and $\lambda_{max,em}$ were measured in acetonitrile solution; [b]$\lambda_{int}$ is the wavelength at the intersection of the absorption and emission spectra; [c]$E_g$ was calculated by the equation of $E_g = 1240/\lambda_{int}$; [d]Redox potentials were calibrated versus ferrocene ($E_{Fc/Fc^+}$) as a reference; [e]$E_{HOMO} = -4.8 - E^{ox}_{onset}$ and $E_{LUMO} = E_{HOMO} + E_g$; [f]$E_{HOMO}$ and $E_{LUMO}$ were estimated from UPS spectra.

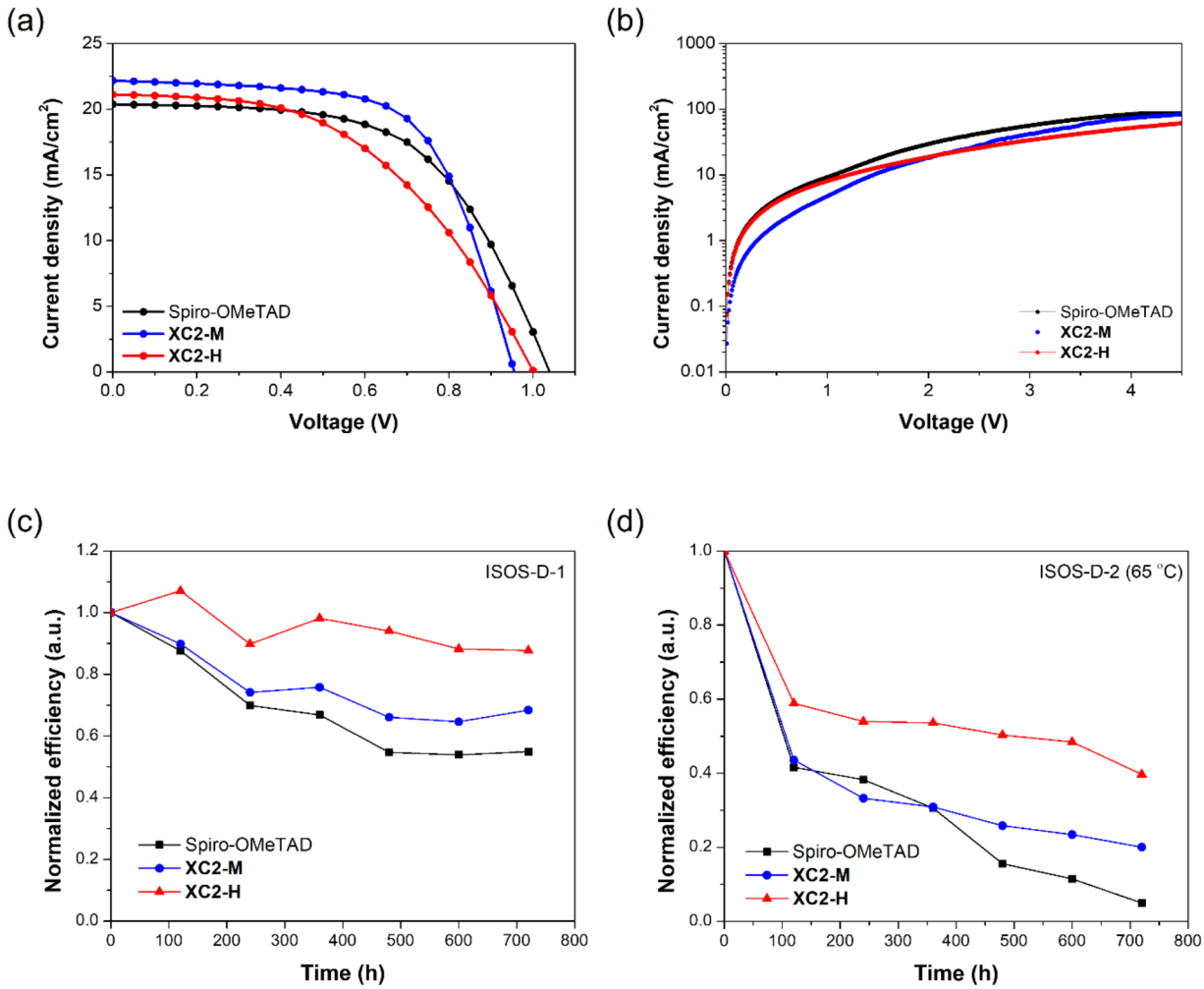


**Fig. 4**. (**a**) *J*–*V* curves from reverse scans of the best cells using **XC2-M**, **XC2-H**, and spiro-OMeTAD with an active area of 0.04 $cm^2$. (**b**) *J*–*V* characteristics of **XC2-M**-, **XC2-H**-, and spiro-OMeTAD-based hole-only devices. (**c**) Normalized power conversion efficiency decay for PSCs (ISOS-D-1) under dark ambient conditions with RH of 30–40%. (**d**) Thermal stability test (ISOS-D-2) at 65 °C in the dark under ambient conditions.

| HTMs | $J_{sc}$ [mA $cm^{-2}$] | $V_{oc}$ [V] | FF | $R_s$ [Ω $cm^2$] | PCE [%] (Champion) | Retaining PCE [%] (after 30 days) |
|---|---|---|---|---|---|---|
| **XC2-M** | 17.4 ± 3.0 | 0.97 ± 0.03 | 0.68 ± 0.07 | 11.3 ± 2.0 | 11.4 ± 1.3 (13.5) | 68 |
| **XC2-H** | 20.1 ± 1.1 | 1.00 ± 0.01 | 0.46 ± 0.03 | 19.5 ± 2.4 | 9.18 ± 0.9 (10.2) | 88 |
| Spiro-OMeTAD | 16.9 ± 3.3 | 1.02 ± 0.01 | 0.63 ± 0.12 | 13.6 ± 3.9 | 10.5 ± 1.0 (12.2) | 55 |

**Table 2**. Photovoltaic parameters determined from *J*–*V* measurements of PSCs based on **XC2-M**, **XC2-H**, and spiro-OMeTAD as HTMs.

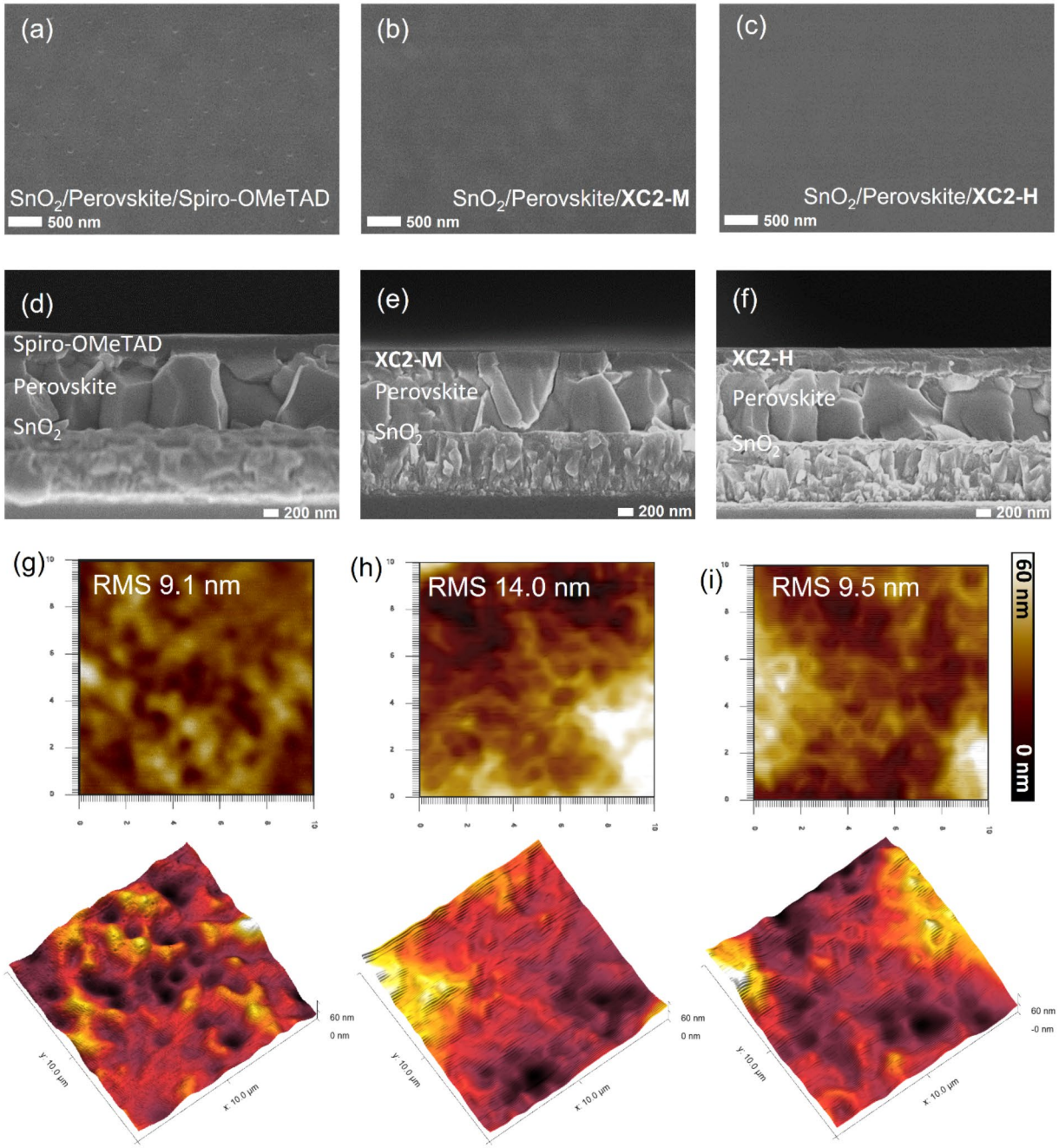


**Fig. 5**. Top-view SEM, cross-section SEM, and AFM morphology images (Z-scale = 60 nm) of FTO/$SnO_2$/perovskite/spiro-OMeTAD (**a**, **d**, and **g**, respectively), FTO/$SnO_2$/perovskite/**XC2-M** (**b**, **e**, and **h**, respectively), and FTO/$SnO_2$/perovskite/**XC2-H** (**c**, **f**, and **i**, respectively). The AFM scan size is 10 μm × 10 μm for all conditions.

analyzer) with a platinum counter electrode, a $Ag/Ag^+$ reference electrode, and a glassy carbon working electrode in 0.1 M tetrabutylammonium hexafluorophosphate ($TBAPF_6$) in $CH_2Cl_2$ solution at a scan rate of 100 mV $s^{-1}$. Ferrocene/ferrocenium ($Fc/Fc^+$) was used as the internal standard. Band diagram data were obtained by performing ultraviolet photoelectron spectroscopy (UPS) measurement using synchrotron radiation at the

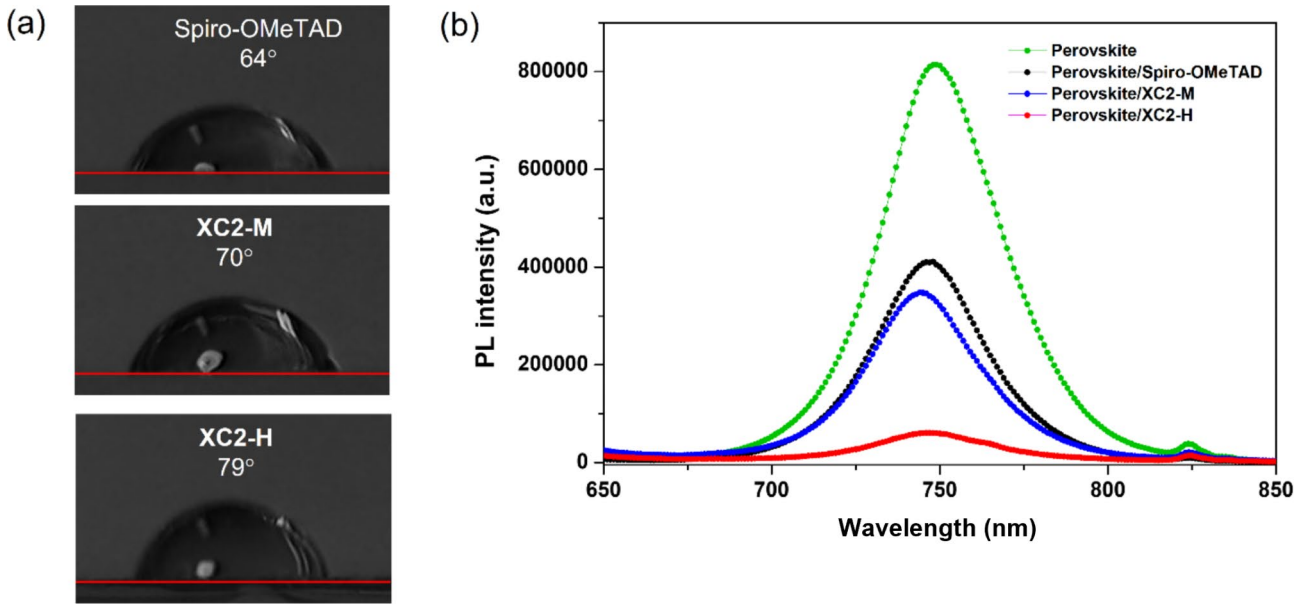


**Fig. 6**. (**a**) Water contact angles of **XC2-M**-, **XC2-H**-, and spiro-OMeTAD-based perovskite films on FTO substrates. (**b**) Steady-state PL spectra of the perovskite films with and without HTMs.

Beamline 3.2Ua. The measurements were conducted under the electrical bias of −9.51 V, an incident light energy of 60 eV, and a scan step resolution of 0.02 eV at Synchrotron Light Research Institute (Thailand). A light source, specifically a high-quality AAA-class 7520-LED with an LSS-7120 LED controller (VeraSol), was used to deliver 1 sun irradiation at an intensity of 100 mW $cm^{-2}$. The light intensity was calibrated using a silicon diode (Hamamatsu S1133). Solar cell performance and stability test were carried out using a Keithley 2400 source meter under 1 sun irradiation conditions with an active cell area of 0.04 $cm^2$, as summarized in Table S2. These solar cells featured carbon electrodes in conjunction with FTO electrodes. Photocurrent density−voltage (*J*−*V*) curves were recorded within a voltage range of 1.10 V to −0.10 V with a scan step of 0.05 V and a delay time of 0 s. The measurements were taken at room temperature under ambient air, and no protective encapsulation was used. Hole mobility was investigated via the space-charge-limited current (SCLC) method using a diode configuration of FTO/poly(3,4-ethylenedioxythiophene): poly(styrenesulfonate) (PEDOT: PSS)/triple-cation perovskite/HTM/C. The detailed analysis method can be found in the supplementary data. Surface and cross-sectional morphology was observed by field emission scanning electron microscopy (FESEM; JSM7610FPlus JEOL, tungsten filament electron source, 20 kV, and secondary electron mode). Topography images were done via atomic force microscopy (AFM, Park NX-10) installed using a non-contact probe (ACTA) with a spring constant k = 37 N $m^{-1}$ and a resonance frequency of 300 kHz. All samples were scanned at a speed of 0.5 µm $s^{-1}$ with a 4 nm set point.

## Synthesis of the HTMs

*Synthesis of* **XC2-M**

A mixture of $N^2$,$N^7$-bis(4-methoxyphenyl)spiro[fluorene-9,9'-xanthene]-2,7-diamine (**3**) (360.2 mg, 0.63 mmol), **5** (342.5 mg, 1.32 mmol), $Pd_2(dba)_3$ (5.8 mg, 0.006 mmol), Xphos (12.0 mg, 0.025 mmol), and *t*-BuONa (168.7 mg, 1.76 mmol) was added in an oven-dried round-bottom flask. The mixture was evacuated and backfilled with $N_2$ gas for three cycles. Freshly distilled toluene (2.6 mL) was added to the mixture, which was then heated to reflux at 120 °C for 4 h under a nitrogen atmosphere. After cooling down to room temperature, water was added and the reaction mixture was extracted with ethyl acetate. The combined organic phase was washed with brine, and dried over anhydrous $Na_2SO_4$. After solvent removal *in vacuo*, the residue was further purified by silica gel column chromatography (20% ethyl acetate in hexane) to afford the analytically pure **XC2-M** as a yellow solid (405.3 mg, 69% yield). $^1$H NMR (400 MHz, $d_6$-DMSO): δ (ppm) = 7.89 (d, *J* = 7.8 Hz, 2H, aromatic), 7.78 (d, *J* = 2.1 Hz, 2H, aromatic), 7.55 (dd, *J* = 14.6 Hz, *J* = 8.3 Hz, 4H, aromatic), 7.45–7.40 (m, 4H, aromatic), 7.15 (dt, *J* = 22.7 Hz, *J* = 7.5 Hz, 4H, aromatic), 7.05 (dd, *J* = 8.7 Hz, *J* = 2.1 Hz, 2H, aromatic), 7.01–6.91 (m, 8H, aromatic), 6.80–6.76 (m, 4H, aromatic), 6.71 (dd, *J* = 8.4 Hz, *J* = 2.2 Hz, 2H, aromatic), 6.62 (d, *J* = 2.2 Hz, 2H, aromatic), 6.58 (d, *J* = 7.8 Hz, 2H, aromatic), 3.81 (s, 6H, $CH_3$), 3.69 (s, 6 H, $CH_3$). $^{13}$C NMR (100 MHz, $d_6$-DMSO): δ (ppm) = 155.39, 154.61, 150.49, 148.08, 141.09, 140.56, 138.86, 137.60, 131.47, 128.35, 127.25, 126.21, 125.93, 125.23, 124.50, 123.68, 122.70, 121.53, 120.49, 120.02, 119.15, 118.57, 117.06, 116.39, 115.51, 114.76, 110.17, 109.18, 55.19, 53.61, 29.03. HRMS (ESI) m/z: calcd for $[M]^+$, $C_{65}H_{48}N_4O_3$ 932.3726; found, 932.3727.

*Synthesis of* **XC2-H**

A mixture of $N^2$,$N^7$-bis(4-methoxyphenyl)spiro[fluorene-9,9'-xanthene]-2,7-diamine (**3**) (200.97 mg, 0.35 mmol), **6** (240.0 mg, 0.73 mmol), $Pd_2(dba)_3$ (3.2 mg, 0.0035 mmol), Xphos (6.67 mg, 0.014 mmol), and *t*-BuONa

(94.2 mg, 0.98 mmol) was added in an oven-dried round-bottom flask. The mixture was evacuated and backfilled with $N_2$ gas for three cycles. Freshly distilled toluene (2.6 mL) was added to the mixture which was then heated to reflux at 120 °C for 4 h under a nitrogen atmosphere. After cooling down to room temperature, water was added and the reaction mixture was extracted with ethyl acetate. The combined organic phase was washed with brine, and dried with anhydrous $Na_2SO_4$. After complete solvent removal, the residue was purified by silica gel column chromatography (20% ethyl acetate in hexane) to afford the analytically pure **XC2-H** as a dark-yellow solid (262.7 mg, 70% yield). $^1$H NMR (400 MHz, $d_6$-DMSO): δ (ppm) = 7.83 (d, $J$ = 7.8 Hz, 2H, aromatic), 7.75 (d, $J$ = 2.1 Hz, 2H, aromatic), 7.50 (d, $J$ = 8.4 Hz, 4H, aromatic), 7.39–7.36 (m, 4H, aromatic), 7.16–7.05 (m, 4H, aromatic), 7.01–6.89 (m, 10H, aromatic), 6.76–6.68 (m, 6H, aromatic), 6.63 (br d, 2H, aromatic), 6.57 (dd, $J$ = 8.1 Hz, $J$ = 1.6 Hz, 2H, aromatic), 4.29 (t, $J$ = 7.1 Hz, 4H, $NCH_2$), 3.69 (s, 6H, $CH_3$), 1.71 (t, $J$ = 7.1 Hz, 4H, $CH_2$), 1.22 (ddt, $J$ = 20.1 Hz, $J$ = 14.3 Hz, $J$ = 8.4 Hz, 12H, $CH_2$), 0.89–0.70 (m, 6H, $CH_3$). $^{13}$C NMR (100 MHz, $d_6$-DMSO): δ (ppm) = 155.80, 155.01, 151.00, 148.53, 140.98, 140.95, 139.27, 137.35, 131.93, 128.70, 127.65, 126.63, 126.31, 125.72, 124.86, 123.21, 122.04, 120.94, 120.41, 119.66, 118.92, 117.45, 116.79, 116.11, 115.16, 110.60, 109.69, 55.59, 54.09 ,42.79, 31.41, 28.95, 26.59, 22.45, 14.28. HRMS (ESI) m/z: calcd for $[M-H]^+$, $C_{75}H_{68}N_4O_3$ 1073.5364; found, 1073.5311.

## Device fabrication

*Preparation of perovskite solutions*. Stock solutions of 1.5 M CsI in dimethyl sulfoxide (DMSO), 1.5 M $PbBr_2$ in a 1:4 (v/v) DMSO: *N*,*N*-dimethylformamide (DMF), 1.5 M $PbI_2$ in a 1:4 (v/v) DMSO: DMF were prepared one day prior to use. A separate formamidinium lead iodide ($FAPbI_3$) solution was prepared by mixing 198.6 mg formamidinium iodide (FAI) with the $PbI_2$ stock solution containing 9% $PbI_2$ powder excess. Similarly, a methylammonium lead tribromide ($MAPbBr_3$) solution was created by mixing 38.6 mg $CH_3NH_3Br$ (MABr) with 9 mol% $PbBr_2$ excess. It has been reported that incorporating excess $PbI_2$ and $PbBr_2$ into the perovskite precursor solution passivates defect, facilitates charge extraction, and consequently improves overall device performance[26,27]. These $FAPbI_3$ and $MAPbBr_3$ solutions were then combined in a 23:77 volume ratio to form a double-cation solution. The triple-cation perovskite solution with the formula $Cs_{0.05}FA_{0.73}MA_{0.22}Pb(I_{0.77}Br_{0.23})_3$ was prepared by combining the double-cation solution with 5 vol% of the CsI stock solution to prevent perovskite phase separation. The resulting triple-cation perovskite solution was kept under constant stirring at room temperature for 1 h and then filtered with 0.22 µm PTFE CNW syringe filter prior to film fabrication.

*Preparation of HTM solutions*. To prepare each HTM solution (spiro-OMeTAD, **XC2-M**, and **XC2-H**), 1 mL of 65.3 mM HTM in chlorobenzene was mixed with 17.5 µL LiTFSI solution (520 mg in 1 mL acetonitrile) and 28.5 µL of 4-*tert*-butylpyridine (*t*-BP). HTM solutions were stirred overnight at room temperature in a glove box.

*Device fabrication*. The PSC devices were fabricated using a previously reported method[15,28–32]. FTO glass substrates were cleaned sequentially using ultrasonication in Alconox solution, deionized (DI) water rinse, and isopropanol rinse. The cleaned substrates were treated with UV-ozone for 20 min to further enhance surface cleanliness. To obtain a compact layer of $SnO_2$ on FTO, a solution of 0.2 M $SnCl_2{\cdot}2H_2O$ in ethanol (EtOH) was prepared and aged at room temperature for 2 days before use. This $SnO_2$ precursor solution was spin-coated onto the FTO substrates at 3000 rpm for 30 s with an acceleration of 1500 rpm/s under ambient conditions. The spin-coated film was then annealed at 180 °C for 1 h and allowed to cool to room temperature. Deposition of the perovskite layer onto the FTO/$SnO_2$ substrates was achieved by spin-coating 50 µL of the triple-cation perovskite solution at 3500 rpm for 35 s with an acceleration rate of 700 rpm $s^{-1}$. Anisole (100 µL) was added onto the rotating substrate as an antisolvent at 30th s after the program started. The film was subsequently thermally treated at 100 °C for 30 min. All spin coating and annealing processes were performed in a glove box filled with $N_2$. 50 uL of the HTM solution was spread and rested on the perovskite layer for 30 s. The deposition of the hole transporting layer was achieved using spin coating for 30 s at a spin speed of 2000 rpm with an acceleration of 1000 rpm $s^{-1}$. To prepare a carbon electrode, the ethanol solvent interlacing technique was used following the previously reported procedure[33,34]. A commercial carbon ink was first coated on a glass slide using a doctor blade to form a carbon electrode with a 80-µm thickness and soaked in ethanol for two hours. The carbon film was peeled off the glass substrate, dried at room temperature, and cut into 0.04 $cm^2$-sheets for further use. To complete the fabrication, the device with all stacking layers was pressed and annealed at 60 °C for 5 min[33,34].

# Results and discussion

## Synthesis of HTMs

The new spiro-based HTMs exhibit a simple structure consisting of the central SFX core attached to two diarylamine arms with *N*-methyl- or *N*-hexylcarbazole, as presented in Fig. 1. The synthetic routes of **XC2-M** and **XC2-H** are shown in Fig. 2 and detailed synthetic procedures and material characterization are available in the Supporting Information (Figs. S1–S2). *N*-Alkylcarbazole (**5** and **6**) and 2,7-dibromospiro[fluorene-9,9'-xanthene] (**2**) were prepared according to the literature[12,35]. *p*-Anisole fragment was then introduced to yield the intermediate **3** through palladium-catalyzed Buchwald–Hartwig amination. The final products were also synthesized by Buchwald–Hartwig amination, giving **XC2-M** and **XC2-H** with the isolated yields of 69% and 70%, respectively. The overall yields of these three-step syntheses are 38% and 42%, respectively. According to green-chemistry protocols, **XC2-M** and **XC2-H** were prepared without inert atmosphere and toxic reagents, lowering unfavorable environmental impact. Notably, these HTMs exhibit exceptional stability under ambient conditions, eliminating the need for glovebox storage in contrast to spiro-OMeTAD. Structures of the synthesized HTMs were characterized using standard spectroscopic techniques such as $^1$H NMR, $^{13}$C NMR, and UV–vis. High-resolution mass spectrometry (HRMS) confirmed the presence of **XC2-M** and **XC2-H**.

In terms of solubility, both new HTMs showed good solubility in various organic solvents, such as dichloromethane, ethyl acetate, acetonitrile, toluene, anisole, as well as in chlorobenzene as shown in Fig. S3c. This is likely caused by the perpendicular spiro-core structure of SFX[15]. Furthermore, calculated costs for the

synthesis of **XC2-M** and **XC2-H** are estimated to be about 120 USD/grams and 140 USD/grams, respectively, whereas spiro-OMeTAD costs are approximately 310 USD/grams (Table S4 and S5). This cost-competitiveness suggests the potential for mass production of **XC2-M** and **XC2-H**, making them more economically viable alternatives to spiro-OMeTAD.

## Optical properties and electron density distribution analysis

Figure 3a shows the UV-vis absorption and fluorescence spectra of **XC2-M**, **XC2-H**, and spiro-OMeTAD in acetonitrile solution at room temperature, and Table 1 summarizes the corresponding spectral data. The optical bandgap ($E_g$) was estimated from the intersection of the absorption and emission bands[36]. The maximum absorption bands ($\lambda_{max,\ abs}$) of **XC2-M** and **XC2-H**, located at 374 nm, correspond to the π−π* transition of the entire π−conjugated backbones. These absorption bands exhibit a slight blue shift compared to that of spiro-OMeTAD (377 nm), which is likely attributed to the highly twisted geometries of the arylamine side groups. The results indicate that the substitution of a methyl group with the hexyl group on carbazole moieties causes no significant change in the absorption properties. The absorption spectra of the HTM films are presented in Fig. S3a (Supporting Information). In their film state, both **XC2-M** and **XC2-H** exhibit a slight red shift in their maximum absorption wavelength, suggesting the formation of *J*-aggregates, a common phenomenon observed in π-conjugated molecules. Minimal light absorption by these HTMs in the visible region (> 430 nm) indicates a minimal impact on the overall light harvesting efficiency of the resulting devices. In addition, no significant changes in the absorption edges of the perovskite films modified with spiro-OMeTAD and the new HTMs were observed (Fig. S3b).

To further study the effect of the alkyl-terminated carbazole units on the structural and electronic properties of the new HTMs, density functional theory (DFT) calculations and time-dependent density functional theory (TDDFT) were performed with B3LYP and CAM-B3LYP functionals, respectively, including 6-31G(d) basis set. Table S1 and Fig. S8 illustrate the highest occupied molecular orbitals (HOMOs) and the lowest unoccupied molecular orbitals (LUMOs) involved in the electron transitions of **XC2-M** and **XC2-H**. The calculation results reveal that the HOMOs of both HTMs are predominantly localized on the central fluorene core with some extensions to the adjacent aromatic rings of the peripheral units, while their LUMOs spread mainly over the fluorene core with some extensions to the carbazole. This implies that charge transfer in these new HTMs occurs from the peripheral OMe-phenyl groups towards the central SFX core and peripheral carbazole units. Furthermore, **XC2-M** and **XC2-H** form similar dihedral angles of ca. −33° and −144° between the fluorene cores attached to phenyl rings and carbazole units, respectively (Fig. 1b), leading to their similar absorption properties (Fig. S7). The result is in good agreement with their UV−vis data in which the new HTMs exhibit the absorption bands at the same wavelength. Significantly, both **XC2-M** and **XC2-H** show twisting motions of *N*-alkylated arylamine side arms and highly distorted, "butterfly-like", spatial structures due to the SFX core unit. This unique shape further reduces intermolecular interactions between HTM molecules, ultimately enhancing their overall solution processability.

## Electrochemical properties

To understand how efficiently the HTMs extract charge carriers, cyclic voltammetry (CV) measurements were performed in dichloromethane solution (Fig. 3b). The experiments were conducted in $TBAPF_6/CH_2Cl_2$ in the presence of ferrocene/ferrocenium ($Fc/Fc^+$) redox couple as an internal standard at a scan rate of 100 mV $s^{-1}$. Redox potentials of **XC2-M**, **XC2-H**, and spiro-OMeTAD are presented in Table 1. **XC2-M** and **XC2-H** exhibit a similar oxidation wave at an onset potential ($E^{ox}_{onset}$) of 0.27−0.28 eV, whereas the $E^{ox}_{onset}$ of spiro-OMeTAD is 0.33 eV. The cathodic shift of the first oxidation potential of the new HTMs by 0.05 eV compared to spiro-OMeTAD indicates their high electron donating ability, consistent with the TD-DFT results (Fig. S9), leading to the higher HOMO energy. This could be ascribed to the electron donation from the diarylamino side arms. The $E_{HOMO}$ and $E_{LUMO}$ of the HTMs were deduced from the CV curves and absorption spectra as illustrated in Fig. 3c.

The CV measurements reveal that the HOMO energy levels of **XC2-M** and **XC2-H** are very similar, at −5.08 eV and −5.07 eV versus vacuum, respectively. Both HTMs exhibit slightly higher HOMO levels compared to spiro-OMeTAD (by 0.05 eV and 0.06 eV, respectively). Given the carbon electrode's work function of −5.0 eV, efficient hole transfer from the HTMs to the electrode is facilitated (Fig. S3d). The LUMO levels of **XC2-M**, **XC2-H**, and spiro-OMeTAD are calculated to be −2.09, −2.11, and − 2.03 eV, respectively.

To confirm the energy levels of the HTMs, we employed ultraviolet photoelectron spectroscopy (UPS). Figure S4 shows the UPS spectra with the cut-off ($E_{cut\text{-}off}$) and onset ($E_{onset}$) energy. According to the equation: $E_F = E_{cut\text{-}off} - 60$ (synchrotron energy)[17], the HOMO levels of spiro-OMeTAD, **XC2-M**, and **XC2-H** are found to be − 5.07, − 4.95, and − 4.90 eV, respectively. By using the relationship: $E_{HOMO} = E_F - E_{onset}$ and $E_{LUMO} = E_{HOMO} + E_g$[37], the LUMO levels are found to be − 2.00, − 1.97, and − 1.93 eV, respectively. Figure 3c illustrates the UPS results which show the same trend as those obtained from the CV experiments.

In terms of the device performance, it is crucial to consider the alignment of energy levels between the perovskite and the HTM materials. The UPS measurement and Tauc plot exhibit the HOMO and LUMO levels of the triple-cation perovskite of − 5.60 and − 3.94 eV, respectively (Figs. S4−S5). Figure S6a shows the energy levels of all HTMs and the triple-cation perovskite obtained by UPS. The HOMO levels of all three HTMs are higher than HOMO level of the perovskite (−5.60 eV). This result indicates a good match between the HOMO levels of the new HTMs and the perovskite layer, suggesting that **XC2-M**, **XC2-H**, and spiro-OMeTAD can efficiently extract holes from the perovskite layer at the interface. This efficient charge extraction is a critical factor for achieving optimal performance in PSCs. Meanwhile, the deeper LUMO level of perovskite than that of all HTMs is beneficial for blocking electron leakage from the perovskite layer to the HTM layer, resulting in the reduction of non-radiative recombination[38].

## Photovoltaic properties

To evaluate the performance of the new small-molecule HTMs, the device configuration of FTO/$SnO_2$/perovskite/HTM/C was used following the previously reported procedure[39,40]. Spiro-OMeTAD was used as a reference HTM in this study. The current–voltage ($J$–$V$) measurements of the devices based on these HTMs were performed under simulated AM 1.5G conditions (Fig. 4a), and the corresponding photovoltaic parameters are presented in Table 2.

Although spiro-OMeTAD exhibits the higher $V_{OC}$ (1.02 V) than the new HTMs (0.97–1.00 V) due to the deeper HOMO level of spiro-OMeTAD, **XC2-M**-based device yields an impressive PCE of 13.5% with a short-circuit photocurrent density ($J_{SC}$) of 17.4 mA $cm^{-2}$, and a fill factor (FF) of 0.68, compared to 12.2% obtained from the spiro-OMeTAD-based device ($J_{SC}$ = 16.9 mA $cm^{-2}$, FF = 0.63). In contrast, the **XC2-H**-based device shows the lowest performance with a PCE of 10.2% ($J_{SC}$ = 20.1 mA $cm^{-2}$, FF = 0.46). The low PCE of **XC2-H** is clearly a result of the low FF (0.46) and high series resistance ($R_s$) of the device. The observed difference in performance might be due to variations in the interactions between the HTM and perovskite layers. A detailed analysis of these interactions is discussed in the following sections. It should be noted that the PCEs achieved by our new HTM-based devices are comparable to those reported in the literature (Table S6 and S7).

Furthermore, the hole mobility of the new HTMs was studied using the space-charge limited current (SCLC) method described in the Supporting Information. The hole-only devices with the structure of FTO/PEDOT:PSS/Perovskite/HTM/C were prepared and used for the measurement. The hole mobility of **XC2-M**, **XC2-H**, and spiro-OMeTAD were found to be $2.67\times10^{-3}$, $1.27\times10^{-3}$, and $2.55\times10^{-3}$ $cm^2$ $V^{-1}$ $s^{-1}$, respectively (Fig. 4b; Table 1). This is likely caused by the intimate contact between the HTM and perovskite in **XC2-M** and spiro-OMeTAD devices. The inferior hole transfer at the interface between the perovskite and **XC2-H** layers, which is consistent with the initial device performance result, is likely caused by a non-conductive barrier of long alkyl chains in the **XC2-H** molecules that hinders the charge transfer[17]. Despite exhibiting a slightly lower hole mobility compared to **XC2-M**, the exceptional long-term stability of **XC2-H** highlights the importance of factors beyond just efficient hole transport in HTM design for PSCs.

## Stability test

To study the effect of humidity on PSC performances, we examined the devices collected in the dark under ambient air with relative humidity (RH) of 30–40% for 720 h without encapsulation (ISOS-D-1). After 720 h of storage under the ambient air, the PCE value of the spiro-OMeTAD-based device decreases dramatically and retains only approximately 55% of its original value, as shown in Fig. 4c and Table S3 (Supplementary Information). In contrast, the **XC2-M**-based device retained approximately 68% of its initial efficiency, demonstrating superior stability. Remarkably, the **XC2-H**-based device, equipped with peripheral hexyl chains, exhibited the highest stability, retaining an impressive 88% of its initial PCE after 720 h of storage. The high uniformity and homogeneity observed in the **XC2-H** film coating the perovskite layer might explain the good stability results achieved by the device. Furthermore, we further investigate the stability of the non-encapsulated devices at 65 °C following the ISOS-D-2 protocol (Fig. 4d). All devices exhibited a significant decrease in PCE after 120 h, with **XC2-H**-based devices losing approximately 40% and others experiencing a 60% reduction. Previous studies have shown that unsealed PSCs degrade rapidly at high temperatures possibly due to thermal breakdown of the perovskite layer. However, in contrast, our **XC2-H**-based device exhibited remarkable stability. After 720 h of exposure at 65 °C, it retained approximately 40% of its initial PCE. This is probably owing to better hydrophobicity of the **XC2-H**-based hole transport layer compared to those based on **XC2-M** and spiro-OMeTAD, which showed substantial degradation under identical conditions. Notably, the spiro-OMeTAD-based device exhibited the most severe degradation at high temperature, retaining only 5% of its initial PCE after 720 h. These results suggest that the long alkyl chains incorporated into the HTM molecule play a critical role in enhancing the long-term stability of the device.

To further evaluate the properties of **XC2-M** and **XC2-H**, their thermal stability was examined using the differential scanning calorimetry (DSC) and thermogravimetric analysis (TGA). As shown in Fig. S10a in the Supporting Information, **XC2-H** exhibits a glass transition temperature ($T_g$) of 147 °C, surpassing that of **XC2-M** (138 °C). Notably, both new HTMs demonstrated higher thermal stability compared to the benchmark material, spiro-OMeTAD (121 °C)[41]. Figure S10b displays the TGA spectra of the new HTMs. The TGA results also show the same trend in which a decomposition temperature (5% weight loss, $T_{d95}$) of **XC2-H** (410 °C) is significantly higher than $T_{d95}$ of **XC2-M** (354 °C). The results confirm that the incorporation of long alkyl chains enhances the thermal stability of the HTMs, in good agreement with the stability test discussed above.

## Film-forming abilities

To further probe morphological variations in the HTM layers on the perovskite, we employed scanning electron microscopy (SEM) and atomic force microscopy (AFM). We hypothesize that the exceptional long-term stability of **XC2-H** is attributable to its unique film morphology. This morphology is likely influenced by the interaction between the HTM and perovskite layers which results in better contact and charge extraction leading to reducing charge recombination losses at the interface. Figure S6b shows a top-view SEM image of perovskite grains with the average size of ca. 300–400 nm. The cross-section SEM images highlight the smooth surface of multilayer structure consisting of a layer of HTM (ca. 200–250 nm) covering the top of the perovskite layer (ca. 600 nm) for all HTMs (Fig. 5d–f). The combination of sufficient HTM layer thickness to fully encapsulate perovskite grains and the good solubility of the HTMs likely contributes to the formation of smooth HTM films (Fig. 5a–c). While the **XC2-H**-based device displayed the smoothest surface (Fig. 5c), it formed a separate layer on top of the perovskite (Fig. 5f). In contrast, the **XC2-M**- and spiro-OMeTAD-based devices exhibited a more uniform interfacial layer that seemed to blend more seamlessly with the perovskite material (Fig. 5d–e). This intimate contact between the HTM and perovskite could potentially enhance charge extraction in **XC2-M** and spiro-OMeTAD devices,

contributing to their higher initial PCEs. However, their films displayed some imperfections. The **XC2-M** layer contained grain boundaries, cracks, and small surface defects, while tiny pinholes were observed on the film of spiro-OMeTAD. Conversely, **XC2-H** formed a more compact and uniform layer without pinholes. This likely arises from the interdigitation of the hexyl chains within the **XC2-H** film. Furthermore, AFM images (scan area: 10 μm x 10 μm) reveal that both **XC2-H** and spiro-OMeTAD exhibited a smooth surface when deposited on the perovskite crystals, with root-mean-square roughness ($R_q$) values of 9.5 and 9.1 nm, respectively (Fig. 5g–i). However, we can observe some defects and pinholes for the film with spiro-OMeTAD. In comparison, the **XC2-M**-based device exhibited a rougher surface with the $R_q$ value of 14 nm, which could be a result of the defects in morphology (Fig. 5h). Therefore, **XC2-H** obviously forms a more uniform morphology on the perovskite layer than **XC2-M**. These results emphasize the superior film morphology of the long-alkyl chain HTM. This compact morphology significantly reduces water penetration and subsequent perovskite degradation, ultimately contributing to the desirable long-term stability observed in **XC2-H**-based devices.

Furthermore, water contact angle measurements of **XC2-M**-, **XC2-H**-, and spiro-OMeTAD-based perovskite films deposited on FTO substrate were conducted to investigate surface wettability of the new HTMs since a hydrophobic surface is desirable for high-performance PSCs to reduce the penetration of moisture into the perovskite layer[42]. Figure 6 presents the results of the water contact angle measurements of **XC2-M**, **XC2-H** and spiro-OMeTAD, deposited on the perovskite film. The largest water contact angle of 79° was obtained on **XC2-H**, when compared with **XC2-M** (64°) and spiro-OMeTAD (70°). The surface of the device based on **XC2-H** shows the highest degree of hydrophobicity, much better than that of **XC2-M** and spiro-OMeTAD, which can be used to justify its high stability in the long term. Our finding is in accordance with previous reports demonstrating that alkyl chains enhance the hydrophobicity of hole transporting layers, thereby improving PSC device stability[43,44]. The high hydrophobicity of **XC2-H**, arising from its hexyl terminal groups, likely contributes to the exceptional stability of **XC2-H** -based devices. By acting as a protective barrier against moisture, **XC2-H** prevents moisture diffusion into the perovskite layer.

## Charge transfer and transport properties

To investigate the hole-transporting ability and nonradiative recombination losses of the HTMs, the steady-state photoluminescence (PL) spectra of three perovskite/HTM films coated on a bare glass substate were measured. In Fig. 6b, the perovskite film shows an intense emission peak around 750 nm whereas the perovskite/HTM films obviously exhibit the PL quenching. The PL intensity was quenched in the decreasing order by the perovskite/**XC2-H**, perovskite/**XC2-M**, and perovskite/spiro-OMeTAD films, in accordance with the trend of $J_{sc}$ values (Table 2). Remarkably, the perovskite/**XC2-H** film demonstrates a strongest PL quenching effect which is in good agreement with its remarkable $J_{sc}$ of 20.1 mA $cm^{-2}$. This suggests that **XC2-H** is the most efficient HTM in terms of hole extraction at the perovskite/HTM interface when compared with **XC2-M** and spiro-OMeTAD. The results together with the compact film morphology, thermal stability and surface hydrophobicity explain the superior performance of the PSC device based on **XC2-H** in a long term.

## Conclusions

Two new SFX-based HTMs, **XC2-M** and **XC2**-H, incorporating *N*-methylcarbazole and *N*-hexylcarbazole rings, respectively, were synthesized using cost-effective and environmentally-friendly protocols. Both HTMs exhibit similar molecular geometries, comparable electrochemical and photophysical properties but remarkably distinct wettability and film morphology on the perovskite layer, leading to the significant difference in long-term device stability. Compared to the champion PCE of a spiro-OMeTAD-based device using the carbon electrode (12.2%), the initial efficiencies of 13.5% and 10.2% were achieved under the same device structure based on **XC2-M** and **XC2-H**, respectively, in line with the trend of hole mobility as follows: **XC2-M** > spiro-OMeTAD > **XC2-H**. This study reveals that the newly developed HTM with peripheral hexyl chains, **XC2-H**, exhibited the significantly higher water contact angle (78°) compared to **XC2-M** (64°) and spiro-OMeTAD (67°). In addition, **XC2-H** shows effective hole transfer at the perovskite/HTM interface which is in agreement with its remarkable $J_{sc}$ of 20.1 mA $cm^{-2}$. Crucially, stability analysis in the dark at ambient humidity following ISOS-D-1 (room temperature) and ISOS-D-2 (65 °C) shows that the **XC2-H**-based device exhibits the excellent stability, surpassing **XC2-M** and spiro-OMeTAD. The exceptional long-term stability of **XC2-H** highlights the importance of factors beyond just hole transport efficiency in designing HTMs for PSCs.

The success of **XC2-H** can be attributed to its unique combination of properties. Its highly-twisted 3D structure enables good solubility in organic solvents, facilitating spin coating. The resulting films exhibit excellent non-wetting behavior, high thermal stability, and a smooth, compact morphology. These attributes are derived from the presence of peripheral long hexyl chains, which repel moisture and minimize pinholes, ultimately enhancing charge extraction. These characteristics, along with its appropriate energy level alignment, enable **XC2-H** to maintain a high-quality interface with the perovskite layer over time, leading to superior device stability. This finding emphasizes that careful consideration of the HTM's molecular structure and its ability to form a dense, smooth film, in addition to hole mobility and energy levels, is crucial for designing efficient HTMs for high-performance PSCs.

## Data availability

The datasets used and/or analyzed during the current study are available from the corresponding author on reasonable request.

Received: 20 May 2024; Accepted: 30 September 2024
Published online: 15 October 2024

## References


1. Kojima, A., Teshima, K., Shirai, Y. & Miyasaka, T. Organometal halide perovskites as visible-light sensitizers for photovoltaic cells. *J. Am. Chem. Soc.* **131**, 6050–6051 (2009).
2. Nakamura, M. et al. Semi-transparent Perovskite Solar Cells for four-terminal Perovskite/CIGS Tandem Solar cells. *ACS Appl. Energy Mater.* **5**, 8103–8111 (2022).
3. Murugan, P., Hu, T., Hu, X. & Chen, Y. Advancements in organic small molecule hole-transporting materials for perovskite solar cells: past and future. *J. Mater. Chem. A*. **10**, 5044–5081 (2022).
4. Conings, B. et al. Perovskite-based hybrid solar cells exceeding 10% efficiency with high reproducibility using a thin film sandwich approach. *Adv. Mater.* **26**, 2041–2046 (2014).
5. Weber, S. et al. Investigation of NiOx-hole transport layers in triple cation perovskite solar cells. *J. Mater. Sci. Mater. Electron.* **29**, 1847–1855 (2018).
6. Bi, D., Yang, L., Boschloo, G., Hagfeldt, A. & Johansson, E. M. J. Effect of different hole transport materials on recombination in $CH_3NH_3PbI_3$ perovskite-sensitized mesoscopic solar cells. *J. Phys. Chem. Lett.* **4**, 1532–1536 (2013).
7. Snaith, H. J. & Grätzel, M. Enhanced charge mobility in a molecular hole transporter via addition of redox inactive ionic dopant: implication to dye-sensitized solar cells. *Appl. Phys. Lett.* **89**, 262114 (2006).
8. Liu, Y. et al. A dopant-free organic hole transport material for efficient planar heterojunction perovskite solar cells. *J. Mater. Chem. A*. **3**, 11940–11947 (2015).
9. Hawash, Z., Ono, L. K. & Qi, Y. Recent advances in spiro-MeOTAD hole transport material and its applications in organic–inorganic halide perovskite solar cells. *Adv. Mater. Interfaces*. **5**, 1700623 (2018).
10. Lin, P. H., Lee, K. M., Ting, C. C. & Liu, C. Y. Spiro-tBuBED: a new derivative of a spirobifluorene-based hole-transporting material for efficient perovskite solar cells. *J. Mater. Chem. A*. **7**, 5934–5937 (2019).
11. Agafonova, E. E. et al. Stars are aligned: triazatruxene hole transporting material hits the sweet spot to reach 20% efficiency of perovskite solar cell. *Sol Energy Mater. Sol Cells*. **252**, 112168 (2023).
12. Xu, B. et al. A low-cost spiro[fluorene-9,9′-xanthene]-based hole transport material for highly efficient solid-state dye-sensitized solar cells and perovskite solar cells. *Energy Environ. Sci.* **9**, 873–877 (2016).
13. Bi, D. et al. Facile synthesized organic hole transporting material for perovskite solar cell with efficiency of 19.8%. *Nano Energy*. **23**, 138–144 (2016).
14. Maciejczyk, M., Ivaturi, A. & Robertson, N. SFX as a low-cost 'spiro' hole-transport material for efficient perovskite solar cells. *J. Mater. Chem. A*. **4**, 4855–4863 (2016).
15. Xu, B. et al. Tailor-making low-cost spiro[fluorene-9,9′-xanthene]-Based 3D oligomers for perovskite solar cells. *Chem*. **2**, 676–687 (2017).
16. Liu, K. et al. Spiro[fluorene-9,9 0-xanthene]-based hole transporting materials for efficient perovskite solar cells with enhanced stability. *Mater. Chem. Front.* **1**, 100–110 (2017).
17. Zhang, J. et al. The importance of pendant groups on triphenylamine-based hole transport materials for obtaining perovskite solar cells with over 20% efficiency. *Adv. Energy Mater.* **8**, 1701209 (2018).
18. Xie, L. H. et al. Unexpected one-pot method to synthesize spiro[fluorene-9,9′-xanthene] building blocks for blue-light-emitting materials. *Org. Lett.* **8**, 2787–2790 (2006).
19. Zhang, Y., Li, Y., Chen, C., Wang, L. & Zhang, J. Design new hole transport materials for efficient perovskite solar cells by suitable combination of donor and core groups. *Org. Electron.* **49**, 255–261 (2017).
20. Govindan, V., Yang, K. C., Fu, Y. S. & Wu, C. G. Low-cost synthesis of heterocyclic spiro-type hole transporting materials for perovskite solar cell applications. *New. J. Chem.* **42**, 7332–7339 (2018).
21. Zhang, J. et al. Strategy to boost the efficiency of mixed-ion perovskite solar cells: changing geometry of the hole transporting material. *ACS Nano*. **10**, 6816–6825 (2016).
22. Magomedov, A. et al. Self-assembled hole transporting monolayer for highly efficient perovskite solar cells. *Adv. Energy Mater.* **8**, 1801892 (2018).
23. Deng, Z. et al. Design of low crystallinity spiro-typed hole transporting material for planar perovskite solar cells to achieve 21.76% efficiency. *Chem. Mater.* **33**, 285–297 (2021).
24. Wang, J. et al. Tuning an electrode work function using organometallic complexes in inverted perovskite solar cells. *J. Am. Chem. Soc.* **143**, 7759–7768 (2021).
25. Jiang, P. et al. The influence of the work function of hybrid carbon electrodes on printable mesoscopic perovskite solar cells. *J. Phys. Chem. C*. **122**, 16481–16487 (2018).
26. Jacobsson, T. J. et al. Unreacted PbI2 as a double-edged sword for enhancing the performance of perovskite solar cells. *J. Am. Chem. Soc.* **138**, 10331–10343 (2016).
27. Misra, R. K. et al. Effect of halide composition on the photochemical stability of perovskite photovoltaic materials. *ChemSusChem*. **9**, 2572–2577 (2016).
28. Zhang, J. et al. The role of 3D molecular structural control in new hole transport materials outperforming spiro-OMeTAD in perovskite solar cells. *Adv. Energy Mater.* **6**, 1601062 (2016).
29. Yang, X., Wang, H., Cai, B., Yu, Z. & Sun, L. Progress in hole-transporting materials for perovskite solar cells. *J. Energy Chem.* **27**, 650–672 (2018).
30. Calió, L., Amrana Kazim, S., Grätzel, M., & Ahmad, S. Perovskite solar cells hole-transport materials for perovskite solar cells. *Angew C hem Int. Ed.* **55**, 14522–14545 (2016).
31. Ruankham, P., Khambunkoed, N., Kanjanaboos, P., Wongratanaphisan, D. & Sagawa, T. Improved reproducibility of carbon-based cesium/formamidinium perovskite solar cells via double antisolvent drippings in adduct approach. *Org. Electron.* **100**, 106362 (2022).
32. Liu, X. et al. Improvement of Cs-$(FAPbI_3)_{0.85}(MAPbBr_3)_{0.15}$ quality via DMSO-molecule-control to increase the efficiency and boost the long-term stability of 1 $cm^2$ sized planar perovskite solar cells. *Sol RRL*. **3**, 1800338 (2019).
33. Zhang, H. et al. Self-adhesive macroporous carbon electrodes for efficient and stable perovskite solar cells. *Adv. Funct. Mater.* **28**, 1802985 (2018).
34. Yang, Y. et al. High performance carbon-based planar perovskite solar cells by hot-pressing approach. *Sol Energy Mater. Sol Cells*. **210**, 110517 (2020).
35. Samae, R. et al. Effect of thiophene spacer position in carbazole-based dye-sensitized solar cells on photophysical, electrochemical and photovoltaic properties. *Eur. J. Org. Chem.* 3536–3549 (2016). (2016).
36. Klán, P. & Wirz, J. *Photochemistry of organic compounds: from concepts to practice. Photochemistry of organic compounds: from concepts to practice* (Wiley, 2009). https://doi.org/10.1002/9781444300017
37. Wang, S. et al. Strong electron acceptor additive based spiro-OMeTAD for high-performance and hysteresis-less planar perovskite solar cells. *RSC Adv.* **10**, 38736–38745 (2020).
38. Cheng, H. et al. Understanding and minimizing non-radiative recombination losses in perovskite light-emitting diodes. *J. Mater. Chem. C*. **10**, 13590–13610 (2022).
39. Passatorntaschakorn, W. et al. Room-temperature carbon electrodes with ethanol solvent interlacing process for efficient and stable planar hybrid perovskite solar cells. *Energy Rep.* **7**, 2493–2500 (2021).
40. Naikaew, A. et al. Photoexcitation of perovskite precursor solution to induce high-valent iodoplumbate species for wide bandgap perovskite solar cells with enhanced photocurrent. *Sci. Rep.* **13**, 6125 (2023).

41. Jeon, N. J. et al. A fluorene-terminated hole-transporting material for highly efficient and stable perovskite solar cells. *Nat. Energy*. **3**, 682–689 (2018).
42. Chi, W. & Banerjee, S. K. Achieving resistance against moisture and oxygen for perovskite solar cells with high efficiency and stability. *Chem. Mater.* **33**, 4269–4303 (2021).
43. Reddy, S. S. et al. Highly efficient organic hole transporting materials for perovskite and organic solar cells with long-term stability. *Adv. Mater.* **28**, 686–693 (2016).
44. Zheng, L. et al. A hydrophobic hole transporting oligothiophene for planar perovskite solar cells with improved stability. *Chem. Commun.* **50**, 11196–11199 (2014).

## Acknowledgements

JM acknowledges the Development and Promotion of Science and Technology Talents Project (DPST) for her scholarship. We acknowledge the Center of Excellence for Innovation in Chemistry (PERCH-CIC), Ministry of Higher Education, Science, Research, and Innovation.

## Author contributions

J.M. carried out the experiments. P.K., P.N., and U.E. coordinated on data analysis. A.N. and L.S. coordinated on solar cell fabrication. C.S. coordinated on AFM analysis. R.S. and H.N. coordinated on UPS measurement. J.M. and S.K. analyzed the data and wrote the manuscript. S.K. initiated the ideas and supervised the project.

## Funding

This work was financially supported by the Mahidol University (Basic Research Fund: fiscal year 2024). JM acknowledges the Development and Promotion of Science and Technology Talents Project (DPST) for her scholarship. We acknowledge the CIF-CNI grant, Faculty of Science, Mahidol University.

## Declarations

## Competing interests

The authors declare no competing interests.

## Additional information

**Supplementary Information** The online version contains supplementary material available at https://doi.org/10.1038/s41598-024-74735-4.

**Correspondence** and requests for materials should be addressed to S.K.